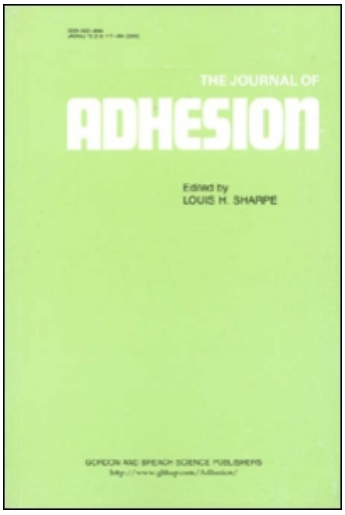

The Journal of Adhesion
Publication details, including instructions for authors and subscription information:
http://www.informaworld.com/smpp/title~content=t713453635

Experimental and Numerical Analysis on Adhesively Bonded Scarf Joints: Effects of the Substrate's Material and Adhesively Bonded Joint Geometry on the Damage Evolution

A. Gacoin[a]; A. Objois[a]; J. Assih[a]; Y. Delmas[a]
[a] Groupe Mécanique, Matériaux, Structures (G.M.M.S.), Université de Reims Champagne Ardenne, Reims cedex, France

To cite this Article Gacoin, A. , Objois, A. , Assih, J. and Delmas, Y.(2008) 'Experimental and Numerical Analysis on Adhesively Bonded Scarf Joints: Effects of the Substrate's Material and Adhesively Bonded Joint Geometry on the Damage Evolution', The Journal of Adhesion, 84: 1, 37 — 59
To link to this Article: DOI: 10.1080/00218460801888375
URL: http://dx.doi.org/10.1080/00218460801888375

The Journal of Adhesion, 84:37–59, 2008

ISSN: 0021-8464 print/1545-5823 online
DOI: 10.1080/00218460801888375

Taylor & Francis
Taylor & Francis Group

Experimental and Numerical Analysis on Adhesively Bonded Scarf Joints: Effects of the Substrate's Material and Adhesively Bonded Joint Geometry on the Damage Evolution

A. Gacoin, A. Objois, J. Assih, and Y. Delmas
Groupe Mécanique, Matériaux, Structures (G.M.M.S.), Université de Reims Champagne Ardenne, Moulin de la Housse, Reims cedex, France

This work characterizes the damage evolution of adhesively bonded scarf joints according to the substrate materials (AU4G-type aluminum alloy and XC18-type steel), the adhesive thickness (ej) and the scarf angle (α). Experimental results were obtained by strain gauge measurements. This method allows distinguishing three damage thresholds, which characterize the damage evolution of the adhesively bonded scarf joint. Contrary to most numerical studies, which determine the strength of the bonded joints according to the ultimate failure load, in this study a failure criterion implemented in ABAQUS was used to predict progressive damage evolution of the adhesively bonded scarf joints. The obtained results show the viability of the numerical model to predict the damage evolution of the bonded joint as a function of the studied key parameters. Nevertheless, for high adhesive thickness or a very low scarf angle the comparison also shows the limits of the numerical model.

Keywords: Adhesively bonded scarf joint; Damage evolution; Finite element model; Strain gauges

1. INTRODUCTION

Bonded structures are present in aeronautical or automotive industries; they are also employed in civil engineering in order to repair concrete structures [1–4]. The first model of adhesive joint behavior was used by Volkersen [5] and subsequently developed by many others [6,7]. Lubkin [8] has clarified the scarf joint mechanical problem. The author has

Received 25 June 2007; in final form 14 December 2007.
Address correspondence to Alexandre Gacoin, GMMS, E.A. 2617, Université de Reims Champagne Ardenne, Moulin de la Housse, BP 1039, F-51687 Reims cedex 2, France. E-mail: alexandre.gacoin@univ-reims.fr

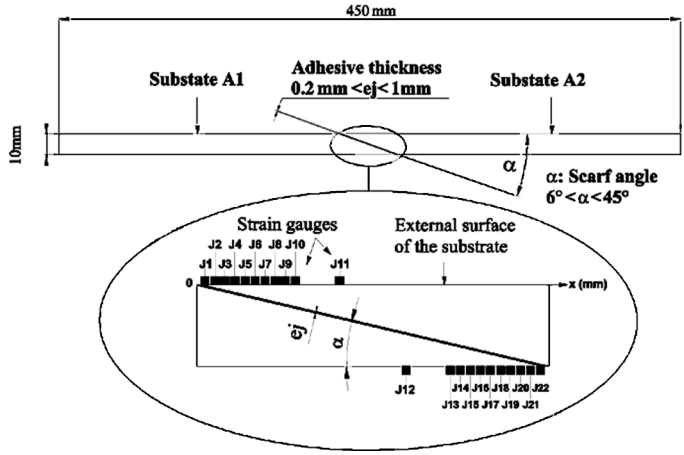

FIGURE 1 Adhesively bonded scarf joint: geometrical specification and location of the electrical strain gauges used to characterize the damage evolution in the adhesively bonded joints.

showed that the stresses were constant along the joint for all scarf angles provided the adherends had the same elastic properties. Nevertheless, the mechanical strength of the bonded joints is impaired by the overstresses near the ends of the substrates and the damage evolves according to the mechanical and geometrical characteristics of the bonded structure [9–13]. Scarf joint bonded structures (Fig. 1) are increasingly being used in industrial applications. Indeed, the rectilinear and continuous shape allows a fast machining of the substrates and unlike the single-lap joints or the tenon and mortise joint [14–18], the adhesive thickness of the adhesively bonded scarf joint is not determined during the machining phase. Moreover, among all the geometries, the adhesively bonded scarf joint is the only one which does not cause bending of substrates which influences the strength of the bonded joints.

Our research works [11,12] have shown in tension, the damage of the adhesively bonded scarf joint is progressive and can be characterized before the ultimate failure by three load thresholds: the initiation of microcracks in the adhesive joint (the load F_i), the start of crack propagation (the load F_p), and the ultimate failure of the adhesive layer (the load F_u). The damage threshold analysis allows characterization of the mechanical performance of the bonded joint. Research clearly shows that the bonded joint's performance strongly depends on various parameters such as the substrate material, the adhesive thickness (ej), and

the scarf angle (α). Nevertheless, technical restrictions limit some experimental research. Indeed, high fluidity of the adhesive before its polymerization does not allow one to make the ej greater than 1 mm, and, as well, a high overlap length is difficult to machine. That is why it is interesting to complete this study by numerical analysis.

Recently, the finite element method (FEM) analysis has been used by several researchers [19–22] to predict the ultimate failure of adhesively bonded joints. However, the determination of F_i is fundamental, because it truly defines the strength of the adhesively bonded joint. In this study, a failure criterion model implemented in ABAQUS is used to predict F_i and the damage evolution of the bonded joints studied.

Our processes rest on the association between the experimental studies and the FEM. Indeed, the experimental results allow concentration on the numerical model in zones of the bonded joint where the first microcracks appear. Then, they allow the check of the validity of the numerical model to predict the actual mechanical behavior of the adhesive joint. We applied this process to study the influence of various key parameters: substrate material, adhesive thickness, and scarf angles.

2. EXPERIMENTAL STUDY

2.1. Samples

Figure 1 and Table 1 show, respectively, the geometrical and mechanical features of the samples. The samples consisted of two substrates A1 and A2 of square section (10×10 mm), made of mild steel with 0.18% carbon (XC18 French Standard) or aluminum alloy (AU4G) and beveled with an angle α. The adhesive is an epoxy resin EPONAL® 317 (commercial name of the French firm CECA, Paris, France). It is a two-component system: an epoxy resin containing mineral fillers and a hardening agent. To obtain a high quality of bonding,

TABLE 1 Mechanical Characteristics of the Adherends and Adhesive

	Aluminum alloy: AU4G	Steel: XC18	Adhesive: EPONAL 317
Young's Modulus (MPa)	72000	210 000	5800
Poisson's ratio	0.31	0.29	0.36
Yield stress (MPa)	300	300	27
Ultimate failure (MPa)	400	400	28.5

it is necessary to impart an optimal roughness to the bonding surfaces. Previous studies have shown that the proper roughness, for the adhesive EPONAL 317, was obtained by sandblasting with alumina particles (AVB 150, Vapour Blast, Tassigny, France) which had a particle diameter of 95 μm. The sandblasting pressure was about 0.5 MPa, the distance from the substrate was 10 cm and the jet was inclined at 45° from the surface. The surface profiles, determined with a roughness probe (HOMMEL TESTER PM2, Hommel-Etamic, Schwenninger, Germany), showed that the average roughness (R_a) was 11 μm. This value was close to the average diameter (d_a) of the mineral fillers ($d_a = 7$ μm) and gave the maximal shear strength of the adhesive joint. The two substrates A1 and A2 were placed on an aligning fixture [12] made in our laboratory, which leads to an optimal alignment between the substrates. The joint thickness was adjusted by means of longitudinal stop screws and gage foil whose thickness was equal to the desired adhesive thickness. A layer of adhesive was spread on the adherends and the substrates were lined up and held in a stable position during 30 days at room temperature.

2.2. Experimental Determination of the Adhesive Layer Damage

The "back-face" technique [23–27] with electrical strain gauges 1/12KY23 HBM (Schenck S.A., Chambourcy, France) was used to measure the microstrains at the external surfaces of the adherends and the disturbances of the strain fields induced by the cracks. The data analysis was carried out in three stages as described in Figs. 2a to c. First, the strain gauges record a linear evolution (a) of the curve $F = f(\varepsilon)$ of applied load *versus* microstrain. In this case, no disturbance is detected, so the adhesive joint is in its elastic range. If a crack occurs in the adhesive joint (b), the microstrain field measured along the external surface of adherends, just above the microcrack, is perturbed. For each strain gauge a change in the slope of the curve, $dF/d\varepsilon$ shows microcrack initiation. Finally, the propagation of the cracks causes stress relaxation (c) which is translated into a change of sign of the slope, $dF/d\varepsilon$. Extensometry makes it possible to locate the zones where the first microcracks appear and the threshold of the crack propagation. The very great difference in stiffness between adherends and adhesive explains that the disturbances located on the curves $F = f(\varepsilon)$ come exclusively from the adhesive joint. A graphic representation (Fig. 3a) determines the variations of the thresholds F_i, F_p, and F_u along the overlap and, thus, the different stages in the gradual damage of the adhesive joint. Among all F_i

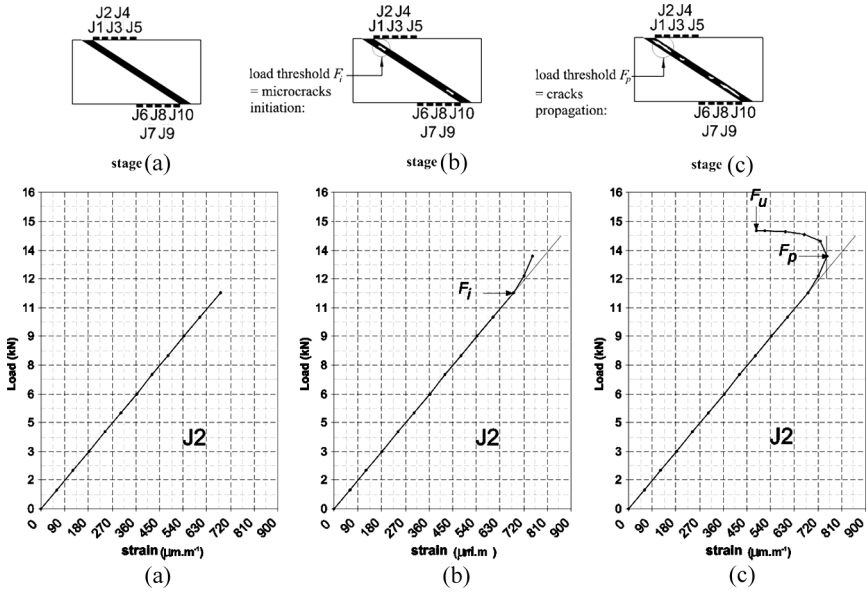

FIGURE 2 Typical experimental load-strain curve for the J_2 gauge, of the back-face technique. (Upper) Different stages of damage evolution in the adhesive joint: (a) no damage, (b) microcracks initiation, and (c) cracks propagation. (Lower) Extensometric method to determine: (a) elastic range, (b) microcracks initiation load F_i, and (c) cracks propagation load F_p and ultimate failure load F_u.

and F_p thresholds, the lowest values (denoted F_{iw} and F_{pw}) are the most important because they represent the beginning of both nonlinear ranges $F_{iw} < F < F_{pw}$ and $F_{pw} < F < F_u$ which define the adhesive joint strength. The histogram (Fig. 3(b)) represents clearly the elastic range $0 < F < F_{iw}$, the microcracks growth range $F_{iw} < F < F_{pw}$, and the cracks propagation range $F_{pw} < F < F_u$.

3. EXPERIMENTAL RESULTS AND DISCUSSION

Duplicate tests (three samples for each parameter studied) show that reproducibility of specimens and, therefore, of measurements is very good; the standard deviation for the threshold of microcracks, the threshold of flaw propagation, and the ultimate failure is around 1% [11,12]. Tensile tests are carried out with a tensile test machine (MTS, Minneapolis, Minnesota), at a very low strain rate (25 N/sec) at room temperature (20 ± 1°C).

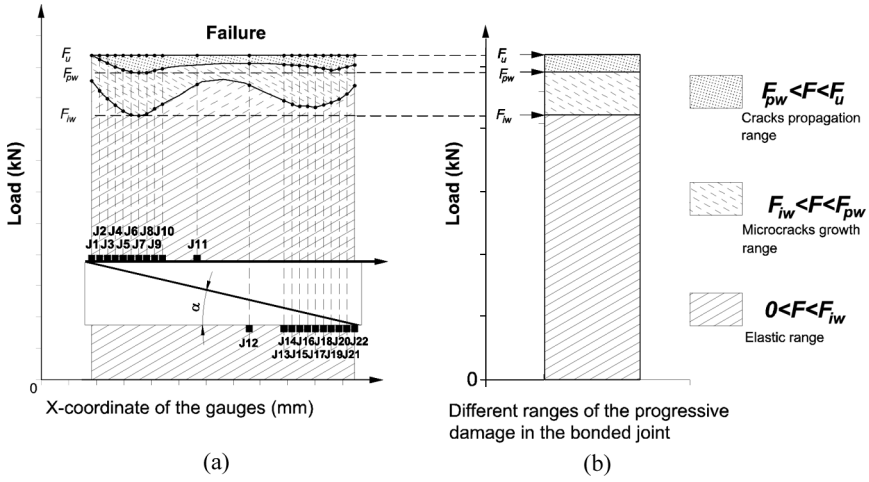

FIGURE 3 (a) Graphic representation of the damage ranges $0 < F < F_{iw}$, $F_{iw} < F < F_{pw}$, and $F_{pw} < F < F_u$ of adhesively bonded scarf joint. Illustration for the case in which the adhesive is 0.2 mm thick and the scarf angle is 33°. (b) Histogram of the damage ranges. Representation of the damage threshold values (F_{iw}, F_{pw}, and F_u) of the adhesive joint.

3.1. Substrate Material Effects

In this section, we check the damage evolution of the adhesive layer according to the substrate material. We have made identical samples ($\alpha = 33°$ and $ej = 0.2$ mm) but the substrate materials are in XC18 steel or AU4G aluminum alloy.

The analysis of the experimental results is interesting because it shows that whatever is the material of the substrates, the adhesive joint's failure is cohesive (failure in the adhesive layer). This tends to show that whatever the substrate material, the strength of the adhesively bonded scarf joint is defined by the intrinsic strength of the adhesive layer that is theoretically constant.

In both cases (XC18 steel and AU4G aluminum alloy), the gauges record the microstrain values in the external surface of the substrate (Fig. 4). The strains are uniform on most of the covering length (3 mm < x < 14 mm) and grow near the substrate extremities (1 mm < x < 3 mm). Note that the microstrains observed near the substrate extremities are higher with the aluminum substrates due to this smaller rigidity. Recently, Qian *et al.* [9] have determined, with a combination of a finite element method and an analytical method based on an independent integral outline, that stress singularities

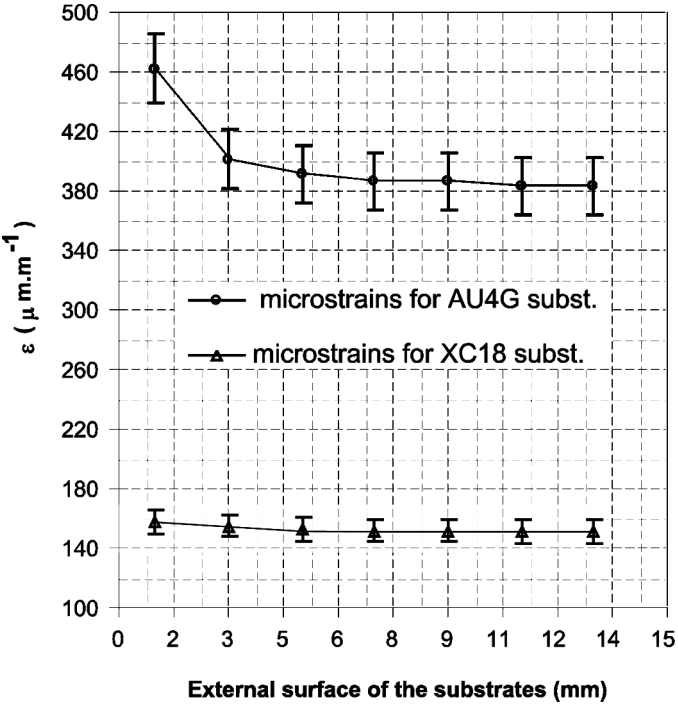

FIGURE 4 Effect of the substrate material (XC18 steel or AU4G aluminum alloy) on the microstrain evolution in the external surface of the substrates. The thickness of the adhesive joint is ej = 0.2 mm, the scarf angle is $\alpha = 33^{\circ}$, and the load is $F = 3$ kN.

are maximal when the difference of rigidity between the substrate and the adhesive is high. We think this stress concentration causes the initiation of the first microcracks and explains the lower strength in tension of the AU4G samples. Indeed, it is interesting to note the effects of these strains on the damage evolution and, more particularly, on the first initiation of microcracks in the adhesive layer. Figure 5 shows the variations of the threshold values F_{iw}, F_{pw}, and F_u. These thresholds correspond to the different ranges which characterize the progressive damage in the adhesively bonded joint according to the substrate material. When the samples are made of AU4G aluminum alloy, the initiation of microcracks occurred for a load $F = 4.35$ kN and with the XC18 substrates, the microcracks are initiated for a load $F = 4.94$ kN. The damage in the adhesively bonded joint appears before in the AU4G case and we can see that all the

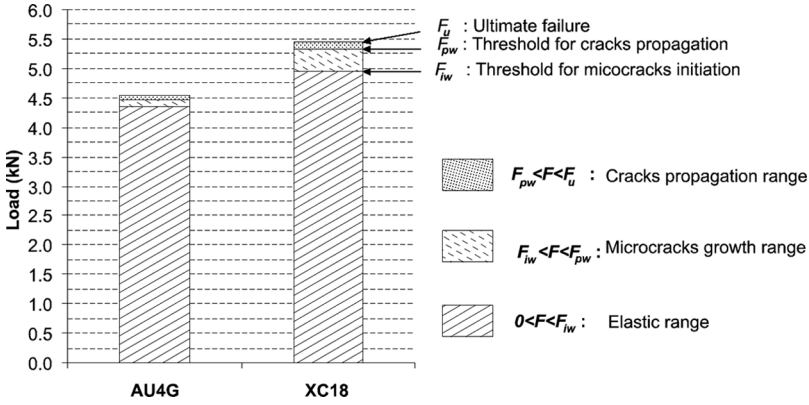

FIGURE 5 Various damage ranges of the adhesively bonded joint. Representation of the first damage threshold values (F_{iw}, F_{pw}, and F_u) when the samples are made of AU4G aluminum alloy or XC18 steel.

thresholds values (F_i, F_g, and F_u) are almost 20% higher with the XC18 substrates.

3.2. Adhesive Thickness Effects

In this section, we check the damage evolution of the adhesive layer according to the adhesive thickness. We vary ej from 0.2 to 1 mm by increments of 0.2 mm. The scarf angle is fixed at $\alpha = 33^\circ$ and the samples are made of XC18 steel.

The experimental results show (Fig. 6) that the microstrains in the external surface of the substrate significantly grow near the extremities of the beveled angle with the increase of the adhesive thickness (ej = 0.2, 0.4, 0.6, 0.8, and 1 mm). Some experimental observations [11] show that the joint's failure is exclusively cohesive (failure at the center of the joint) for thickness lower than 0.3 mm, mixed between 0.4 and 0.7 mm, and then principally adhesive (failure at the interface) from 0.8 mm. We think that other micromechanical phenomena appear when ej increases. The internal stresses in the adhesive layer, resulting from the sample preparation, can evolve with the adhesive joint thickness and so modify the mechanical behavior of the adhesive [28]. The stiffness of the adhesive layer, favorable to the bonded structure, decreases with increases in ej. The eccentricity of the load increases with increasing load and bond thickness and creates stress concentrations in the external surface of the substrates and in the adhesive/adherend interface. Figure 7 highlights this

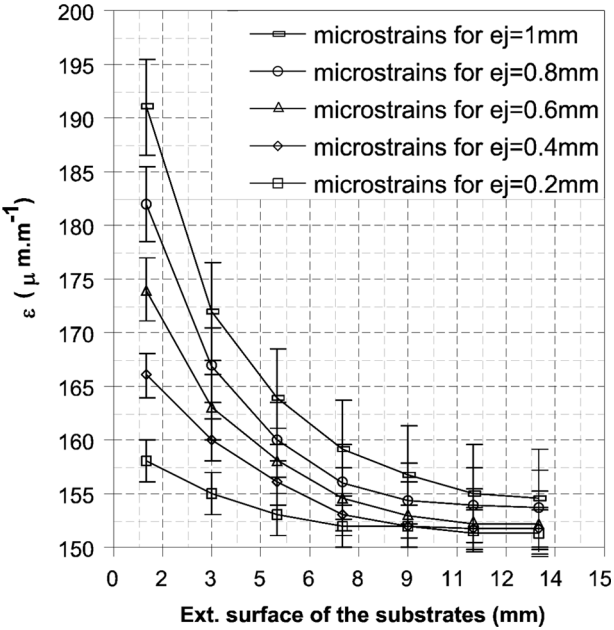

FIGURE 6 Effect of the adhesive thickness (0.2 mm, 0.4 mm, 0.6 mm, 0.8 mm, and 1 mm) on the evolution of the microstrains in the external surface of the substrates. The scarf angle is $\alpha = 33^\circ$ and the load is $F = 3$ kN.

hypothesis. The maximum strength is indeed obtained for ej = 0.2 mm. Then, when ej grows to 1 mm, the performance of the samples defined by the F_{iw}, F_{pw}, and F_u thresholds progressively decrease.

3.3. Scarf Angle Effects

In this section, we check the damage evolution of the adhesive layer according to the scarf angle. We vary the scarf angles ($\alpha = 45^\circ$, 33°, 18°, 10°, and 6°). The adhesive joint thickness is ej = 0.2 mm and the substrates are made of XC18 steel.

The experimental results show (Fig. 8) that the microstrains in the external surface of the substrate significantly grow near the extremities of the beveled angle with the decrease of α (45°, 33°, 18°, 10°, 6°). Figure 9 also shows that this parameter has a very important effect on the damage thresholds evolution F_{iw}, F_{pw}, and F_u.

Indeed, F_{iw} increases when α decreases but stabilizes after 10°. However, F_u continues to increase. So, it can be noticed that for a high

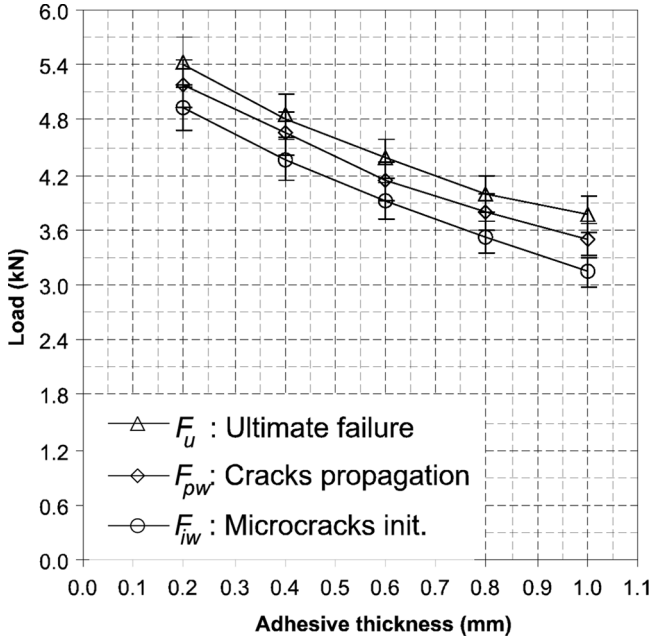

FIGURE 7 Various damage thresholds (F_{iw}, F_{pw}, and F_u) of the adhesively bonded scarf joints when the adhesive thickness is ej = 0.2 mm, 0.4 mm, 0.6 mm, 0.8 mm, and 1 mm.

(45° and 33°) the mechanical behavior shows a significant "brittle" character. Then, when the scarf angle value decreases, the difference between F_{iw} and F_u is more and more important. Indeed, a large length of overlap gives a more uniform distribution of stress within the adhesive joint and, thus, reduces the propagation of cracks in the adhesive layer. This feature gives a "plastic" behavior to the adhesively bonded joint.

4. COMPARISON BETWEEN EXPERIMENTAL AND NUMERICAL RESULTS

4.1. Finite Element Method

For this section, ABAQUS finite element analyses are carried out on various geometric configurations of the adhesively bonded scarf joints in order to assess the numerical prediction of the experimental results. A failure criterion proposed by Saanouni *et al.* [28], described in Section 4.2, is used as a subroutine in the ABAQUS finite element

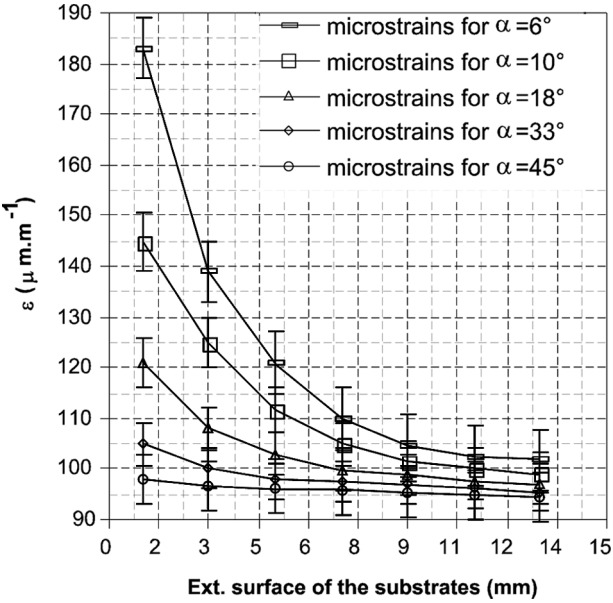

FIGURE 8 Effect of the scarf angle (6°, 10°, 18°, 33°, 45°) on the evolution of the microstrains in the external surface of the substrates. The adhesive thickness is ej = 0.2 mm and the load is $F = 2$ kN.

program [29,30]. The adhesively bonded scarf joints are modeled as a problem in plane strain, with geometric length scales similar to the experimental samples. The calculations are carried out with the elasto-plastic properties of adherends and adhesive (XC18 metal, AU4G aluminum, and EPONAL 317 adhesive) listed in Table 1. The materials are considered as homogenous, isotropic, and the loading rate is $F = 25$ N/s.

Each 2-D model matches the experimental boundary conditions and the experimental loading rate (Fig. 10). The contact between the adhesive joint and the substrates is considered as perfect. The modeled bonded structures are meshed with the Linear Triangular Element (CPE3). In the adhesive joint, the size of elements is 0.1 mm.

4.2. Failure Criteria

The principal aspects of the model [28] are briefly described below. The resolution of the problem describing the large displacement is

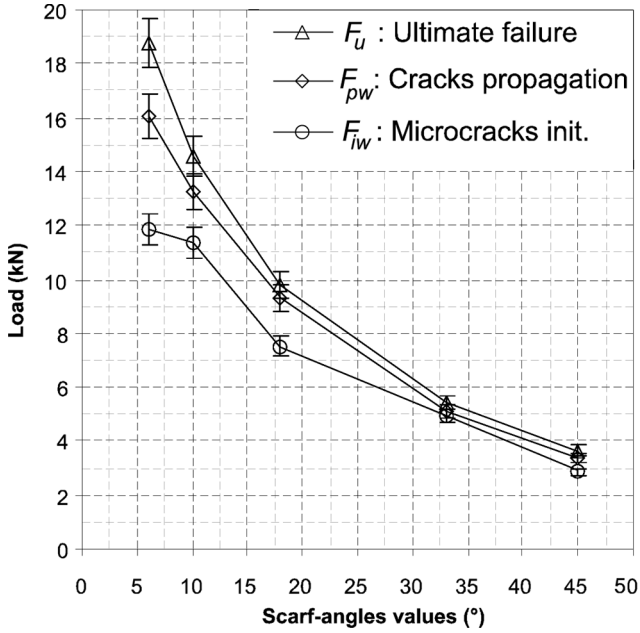

FIGURE 9 Various damage thresholds (F_{iw}, F_{pw}, and F_u) of the adhesively bonded scarf joints when the scarf angle is $\alpha = 6^\circ$, 10°, 18°, 33°, and 45°.

governed by a partial derivative equation. The equilibrium equations are derived from the principle of virtual powers. Thanks to these equations, by using the FEM in displacement (Galerkin [32]), we obtain the nonlinear algebraic system

$$\{[M]\{\ddot{u}\} - \{F(u)\} = 0, \tag{1}$$

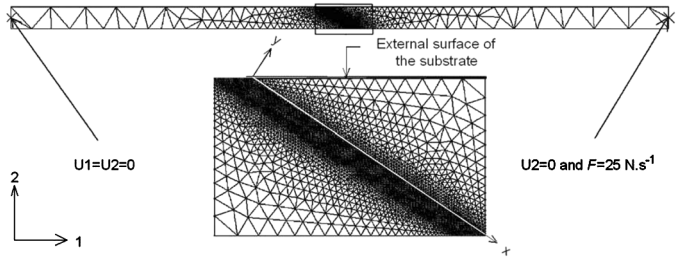

FIGURE 10 Illustration of the boundary conditions and finite element meshing of the scarf joint bonded structure (scarf angle $\alpha = 33^\circ$ and adhesive thickness ej = 0.4 mm).

with [M] being the mass matrix

$$[M] = \sum_j \int_{V^j} \rho [N^k]^T [N^i] dV \tag{2}$$

and {F} the mechanical vector of the applied load

$$\{F(u,T)\} = \sum_j \left\{ - \int_{V^j} [B^k]^T \{\underline{\sigma}\} dV + \int_{V^j} [N^k]^T \{f_d\} dV + \int_{S_F^j} [N^k]^T \{t\} dS + \int_{S_c^j} [N^k]^T [t_c] dS \right\}. \tag{3}$$

In these equations $\{\ddot{u}\}$ is the nodal acceleration vector and $\{u\}$ the displacement vector. The vector $\{f_d\}$ represents the volume forces, the vector $\{t\}$ the surface forces, and the vector $\{t_c\}$ the contact forces. The matrix $[N]$ defines the displacement interpolation functions, $[B]$ their derivatives, and ρ the material density.

To solve the system (1) with regard to displacement (u, v, w), explicit diagrams of resolution are employed by using the ABAQUS software. The resolution is done sequentially on the time interval $[t_n,\ t_{n+1} = t_n + \Delta t]$, according to the system (1).

Resolution of the mechanical problem:

$$\{\ddot{u}_n\} = [M]^{-1} \{F(u_n)\} \tag{4}$$

$$\left\{\dot{u}_{n+\frac{1}{2}}\right\} = \left\{\dot{u}_{n-\frac{1}{2}}\right\} + \frac{\Delta t_{n+1} + \Delta t_n}{2} \{\ddot{u}_n\} \tag{5}$$

$$\{u_{n+1}\} = \{u_n\} + \Delta t_{n+1} \left\{\dot{u}_{n+\frac{1}{2}}\right\}. \tag{6}$$

This explicit strategy of resolution needs a subroutine user VUMAT (in ABAQUS) to calculate σ_{n+1} and t_{cn+1} and in order to evaluate $\{F(u)\}$ [Eq. (3)]. The calculation of the various mechanical fields is carried out by numerically integrating the following differential equations (model of behavior):

for the plastic field

$$\begin{cases} \underline{\sigma} = (1-D)[\lambda_e(\underline{\varepsilon}^e : \underline{1})\underline{1} + 2\mu\underline{\varepsilon}^e] \\ \dot{\underline{\varepsilon}}^e = \dot{\lambda}\dfrac{3}{2}\dfrac{1}{\sqrt{1-D}}\dfrac{\underline{\sigma}^{dev}}{\sqrt{\frac{3}{2}\underline{\sigma}^{dev} : \underline{\sigma}^{dev}}} \end{cases}, \tag{7}$$

for the damage evolution

$$\begin{cases} \dot{\boldsymbol{D}} = \dfrac{\dot{\lambda}}{(1-D)^{\beta}} \left[\dfrac{Y - Y_0}{S}\right]^{s} \\ Y = \dfrac{1}{2}\lambda_e (\underline{\varepsilon}^e : \underline{1})^2 + \mu \underline{\varepsilon}^e : \underline{\varepsilon}^e \end{cases} . \tag{8}$$

In these equations, the various variables are: $\underline{\sigma}$ and $\dot{\underline{\varepsilon}}^p$ the Cauchy stress and the plastic strain-rate tensor respectively: $\dot{\underline{\varepsilon}}$ is the total strain-rate and $\dot{\underline{\varepsilon}}_j^e$ is the elastic strain-rate according to Jaumann [33] $\dot{\underline{\varepsilon}} = \dot{\underline{\varepsilon}}_j^e + \dot{\underline{\varepsilon}}^p$; $(Y, \boldsymbol{D})$ are the damage scalar variables, and D varies between 0 and 1; the coefficients λ_e and μ are the Lamé coefficients; $\underline{\sigma}^{dev}$ is the stress deviator tensor; $\dot{\lambda}$ is the Lagrangian multiplier; and s, S, Y_0 and β are material parameters characterizing the damage evolution. The damage parameters used are $S = 2, s = 1, \beta = 1, Y_0 = 0$ for XC18 steel and $S = 1.10^3, s = 1, \beta = 1, Y_0 = 0.99$ for EPONAL 317 Epoxy. The numerical integration of this system is carried out by an implicit solution after having carried out a reduction in the number of equations [30–31]. The implementation of this model in ABAQUS *via* subroutine VUMAT was made so that the calculation is done with the experimental damage behavior of the adhesive joint.

In order to compare the numerical results with the experimental measurements, we chose to compare the evolution of microstrains along the external surface of the substrate, F_{iw}, and F_u according to the material of the substrates, the adhesive thickness, and the scarf angles.

4.3. Substrate Material

In this section, we check the ability of the numerical model to predict the damage evolution of the adhesive layer according to the material of the substrates. Two identical samples were modeled ($\alpha = 33^\circ$ and ej = 0.2 mm) but with different substrates: XC18 steel or AU4G aluminum alloy.

For both the 2-D models studied, the theory-experiment comparison of microstrains (Fig. 11) is satisfactory because it shows the prediction is good in the external surface of the substrates. The microstrains are uniformly distributed, except for the extreme point of the substrate corner where the gradient of microstrains is very intense.

The first numerical damages appear at the end of bevels (x = 1 mm), as was observed in experiments for the J2 gauge. The numerical microstrains (Fig. 12), perpendicular to the first damaged elements (D = 1) in the adhesive joint give the damage prediction histograms (Fig. 13).

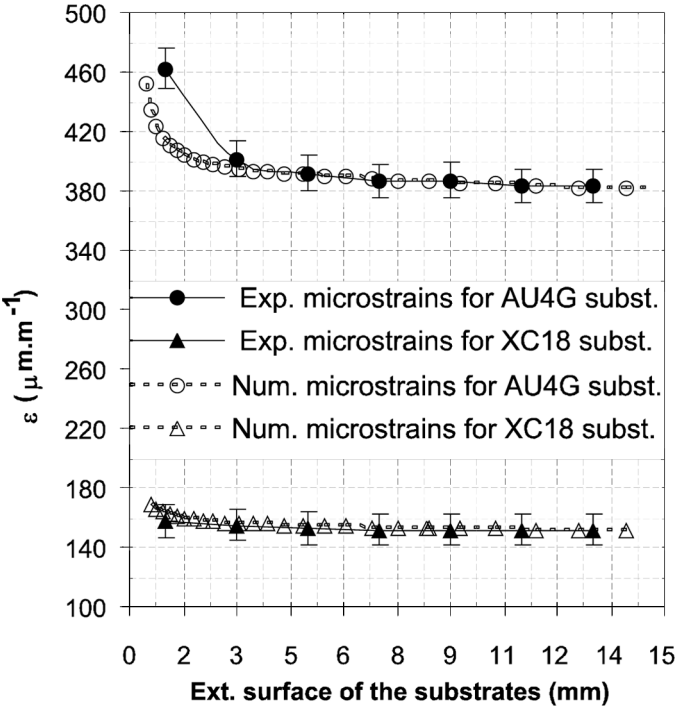

FIGURE 11 Effect of the substrate material (XC18 steel or AU4G aluminum alloy) on the experimental and numerical microstrains evolution in the external surface of the substrates. The scarf angle is $\alpha = 33^{\circ}$ and the load is $F = 3\,\text{kN}$.

The damage prediction by the numerical model is also satisfactory. It shows, with good accuracy, that the damage takes place early when the stiffness of the substrates decreases. The results of numerical modeling support the previously stated hypothesis discussed in Section 3.2. The elevated stiffness of the bonded connection (metal-adhesive-metal), increases the performance of the bonded structure. When the thin adhesive layer is confined between stiff substrates, the substrates constrain the microstrains in the polymer and distribute them in a more homogeneous way in the whole adhesive mass. That confers on the bonded structure a better resistance to damage.

4.4. Adhesive Joint Thickness

In this section, we check the viability of the numerical model to predict the damage evolution of the adhesive layer according to the adhesive

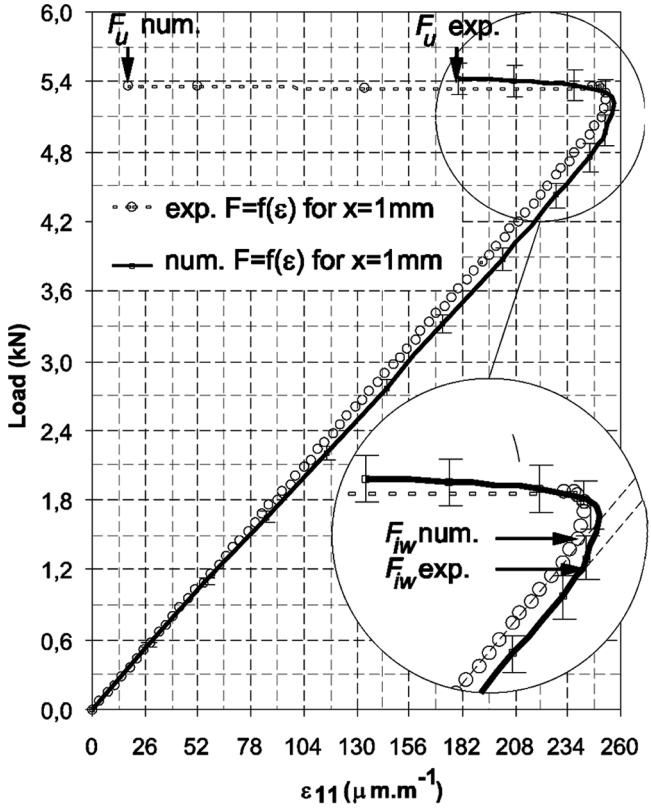

FIGURE 12 Experimental and numerical microstrains at the external surface of the adherend (x = 1 mm) and comparison of the microcrack initiation threshold (F_{iw}) and ultimate failure (F_u). Case in which the scarf angle is $\alpha = 33^\circ$, the adhesive thickness is ej = 0.2 mm, and the substrate material is XC18 steel.

thickness. Five samples were modeled with various adhesive thicknesses: from 0.2 to 1 mm by increments of 0.2 mm. The scarf angle is fixed at $\alpha = 33^\circ$ and the substrates are XC18 steel.

The microstrains obtained by the numerical analysis (Fig. 14) in the external surface of the substrates, for $F = 3$ kN [$F = 3$ kN corresponds to the experimental threshold before which the first microcracks initiate for the most brittle sample (ej = 1 mm)] show that they are very close to the experimental measurements and they also show that the strains are more important, in the extremity of the substrate, when ej increases. The accuracy of the numerical model to predict F_i

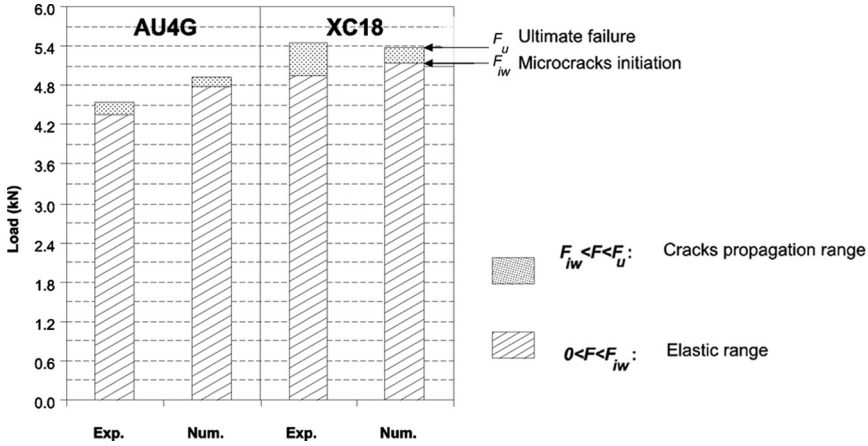

FIGURE 13 Experimental and numerical comparison of the various damage ranges of the adhesively bonded joint. Representation of the damage threshold values (F_{iw}, F_{pw}, and F_u) when the samples are made of AU4G aluminum alloy or XC18 steel.

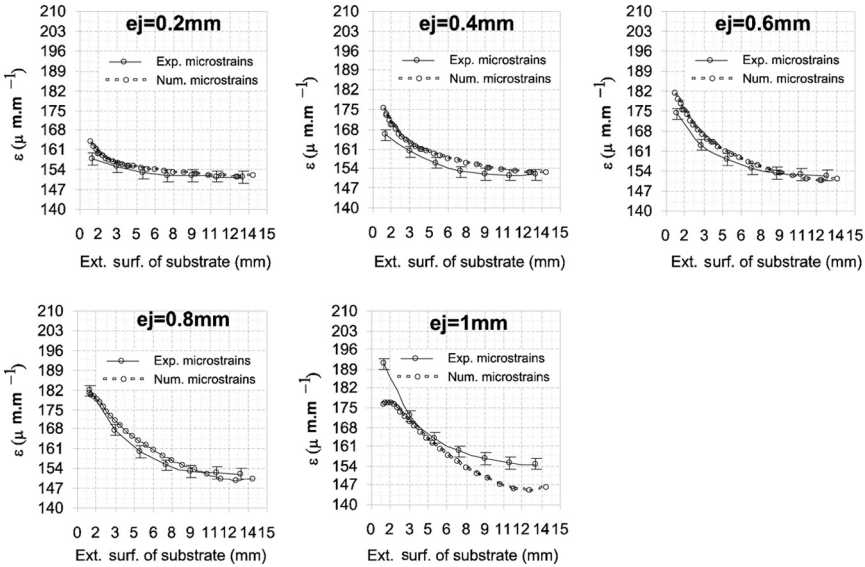

FIGURE 14 Effect of the adhesive thickness on the experimental and numerical microstrains evolution in the external surface of the substrates. The scarf angle value is $\alpha = 33^\circ$ and the load is $F = 3\,\text{kN}$.

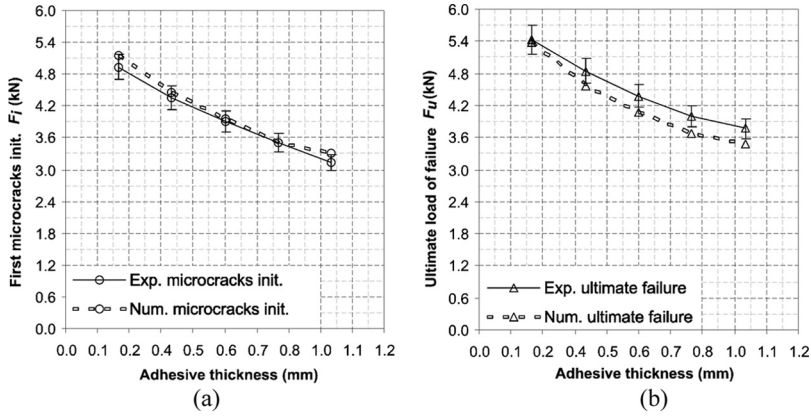

FIGURE 15 Experimental and numerical: (a) first microcracks initiation and (b) ultimate load of failure in the adhesively bonded scarf joint according to the adhesive thickness.

and F_u (Fig. 15) is satisfactory for the most part. The accuracy decreases slightly when becomes large (ej > 0.8 mm).

Figures 16a and b show the FEM adhesive shear stress (σ_{xy}) and normal stress (σ_{yy}) distribution, for different ej; along the overlap nearest to the adherend/adhesive interface. The figures show that

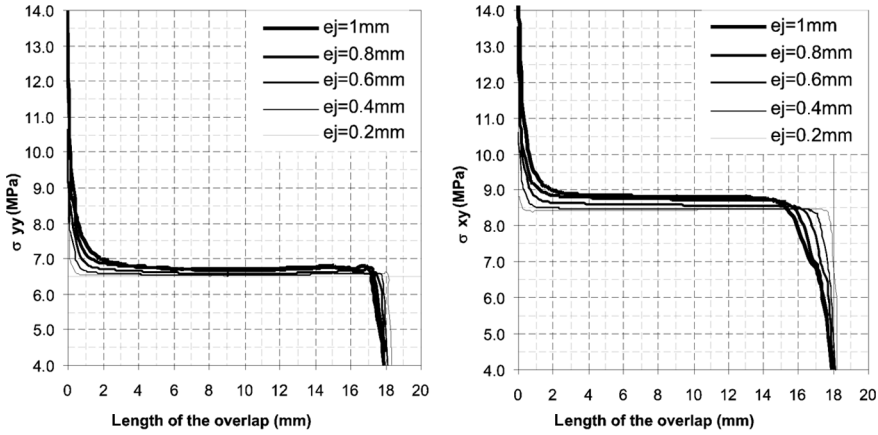

FIGURE 16 Distribution of the (a) normal stresses and (b) shear stresses along the adhesive/adherend interface for different values of the adhesive thickness. The load is $F = 2$ kN.

σ_{xy} and σ_{yy} are uniform over a large part of the overlap except near the edges. Indeed, increasing ej causes a change in the shape of the adhesive layer during the loading and increases the stress concentration at the adherend tip. The FEM prediction confirm the trends observed experimentally.

4.5. Scarf Angle Values

The last point to be checked is the viability of the numerical model to predict the damage evolution of the adhesive layer as a function of the scarf angle. Five samples were modeled with various scarf angles α: 45°, 33°, 18°, 10°, and 6°. The adhesive joint thickness was ej = 0.2 mm and the substrates were XC18 steel.

Figure 17 shows the comparison between experimental and numerical strains in the external surface of the substrates according to the scarf angles, for $F = 2$ kN [$F = 2$ kN corresponds to the experimental threshold before which the first microcracks initiate for the most brittle sample ($\alpha = 45°$)]. The numerical model predicts with good accuracy the increase in the microstrains near the extremities of the substrates, when the scarf angles decrease. The correspondence

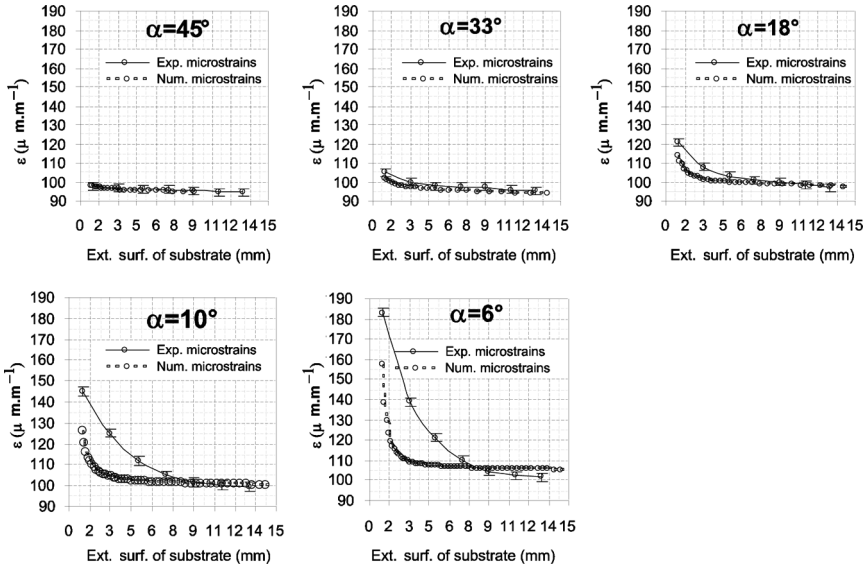

FIGURE 17 Effect of the scarf angle on the experimental and numerical microstrains evolution in the external surface of the substrates. The adhesive thickness is ej = 0.2 mm and the load is $F = 2$ kN.

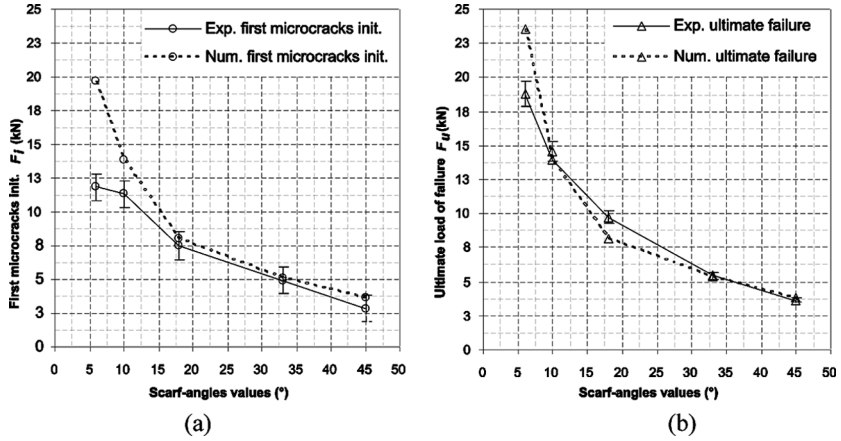

FIGURE 18 Experimental and numerical: (a) first microcracks initiation and (b) ultimate load of failure in the adhesively bonded scarf joint according to the scarf angle.

between experimental and numerical results is satisfactory when α is high ($\alpha = 45^\circ$ or $\alpha = 33^\circ$), but not so when α is very low ($\alpha = 6^\circ$). Figure 18 also shows that the numerical model predicts satisfactorily, for the most part, of samples studied ($18^\circ < \alpha < 45^\circ$), the damage evolution when varies, but a slight inaccuracy appears when becomes very low ($\alpha < 18^\circ$).

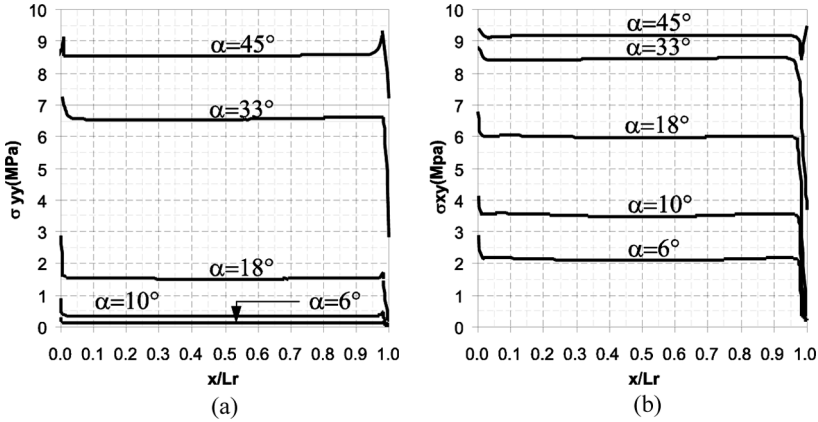

FIGURE 19 Distribution of the (a) normal stresses and (b) shear stresses along the adhesive/adherend interface for different values of the scarf angle. The load is $F = 2\,\text{kN}$ and Lr is the length of the overlap.

Figures 19a and b show the FEM σ_{xy} and σ_{yy} distribution, for different scarf angles, along the overlap nearest to the adherend/adhesive interface. The figures show that σ_{xy} and σ_{yy} are uniform on a large part of the overlap and a large variation of the stress in the adhesive/adherend interface near the edges. Although scarf joints with small scarf angles are especially sensitive to the mismatch between adherend end and adhesive [34,35], small scarf angles (6° and 10°) allow a better distribution of σ_{yy} and σ_{xy} in the adhesive/adherend interface. These results confirm the experimental results which show a better resistance against the propagation of cracking when α is low.

5. CONCLUSION

This work shows the great interest in numerical models, associated with experimental results, to understand and to explain the complex mechanisms which define the mechanical behavior and the damage evolution of the adhesively bonded joints.

The experimental results obtained by the extensometric method show the effects of the substrate material, ej, and the scarf angles on damage evolution of the adhesively bonded scarf joint. The maximal resistance to the damage of the adhesively bonded scarf joints relates closely to the delay of the initiation of microcracks. It appears this condition is obtained in our study when: the substrate is stiff (XC18 steel), the adhesive layer is thin (ej = 0.2 mm), and α is low but, note, not lower than $\alpha = 18^\circ$.

The experimental data directed our work and allowed the comparison with finite element predictions, using a failure criterion. The comparison of theory-experiment data is interesting because it shows the viability of the numerical model to take into account the effects of various parameters and to predict with a good accuracy the real damage evolution of adhesively bonded scarf joints, *i.e.* F_{iw} and F_u.

The comparison also shows the limits of the numerical model to predict the local behavior of the adhesive joint when the geometry becomes complex, *i.e.* for a large ej (ej > 0.8 mm) or a very low α ($\alpha < 18^\circ$). A slight inaccuracy is observed, principally in the prediction of the distribution of the microstrains at the ends of the external surface of the substrates and F_{iw} in the adhesive layer.

Several hypotheses can explain this inaccuracy. Firstly, the mechanical behavior of the adhesive film can evolve with ej because the stresses on the adhesive change with its thickness. Secondly, the adhesive/substrate interface behavior, which is very difficult to predict in experiments and is very sensitive to the mismatch between adherend end and adhesive (when α is low), can be a parameter which

explains this inaccuracy. Thirdly, the ends of the geometric singularities (which are subject to very complex disturbances during the sample preparation) are probably badly interpreted by the numerical model when α is very low.

To continue our work about the damage evolution in the scarf joint bonded structure, it seemed important to integrate the hypotheses above in the numerical model. It will be then possible to predict with a great accuracy, whatever the joint's shape, the complex mechanical behavior induced by geometric singularities and the damage evolution in adhesively bonded joints.

REFERENCES

[1] Li, A., Assih, J., and Delmas, Y., *J. Adhesion Sci. Technol.* **14**, 1639–1656 (2000).
[2] Bourget, M., Delmas, Y., and Toulemonde, F., *Materials and Structures* **34**, 155–162 (2001).
[3] Assih, J., Li, A., and Delmas, Y., *Composites in Constructions* **127**, 623–628 (2001).
[4] Diagana, C., Li, A., Gedalia, B., and Delmas, Y., *Engineering Structures* **25**, 507–516 (2003).
[5] Volkersen, O., *Luftfahrtforschung* **15**, 41–47 (1938).
[6] Goland, M. and Riessner, E., *J. Applied. Mech.* **11**, 17–27 (1944).
[7] Matthews, F. L., Kilty, P. F., and Godwin, E. W., *Composites* **13**, 29–37 (1982).
[8] Lubkin, J. L., *J. Appl. Mech.* **11**, 17–27 (1944).
[9] Qian, Z. Q. and Akisanya, A. R., *Acta Mater.* **46**, 4895–4904 (1998).
[10] Qian, Z. Q. and Akisanya, A. R., *Eur. J. Mech. A. Solids* **18**, 443–463 (1999).
[11] Objois, A., Gilibert, Y., and Fargette, B., *J. Adhesion* **70**, 13–32 (1999).
[12] Objois, A., Fargette, B., and Gilibert, Y., *J. Adhesion Sci. Technol.* **14**, 1057–1070 (2000).
[13] Imanaka, M. and Iwata, T., *Int. J. of Fracture* **80**, 69–76 (1996).
[14] Adams, R. D. and Peppiat, N. A., *J. Strain Anal.* **3**, 185–196 (1974).
[15] Frigyes, T., *J. Adhesion* **7**, 301–309 (1976).
[16] Allman, D. J., *J. Q. Mech. Applic. Math.* **13**, 415–436 (1977).
[17] Fargette, B., Gilibert, Y., and Rimlinger, L., *J. Adhesion* **59**, 159–170 (1996).
[18] Erpolat, S., Ashcroft, I. A., Crocombe, A. D., and Abdel-Wahab, M. M., *Int. J. Fatigue* **26**, 1189–1196 (2004).
[19] Hadavinia, H., Kinloch, A. J., Little, M. S. G., and Taylor, A. C., *Int. J. Adhes. Adhes.* **23**, 463–471 (2003).
[20] Zgoul, M. and Crocombed, A. D., *Int. J. Adhes. Adhes.* **24**, 255–266 (2004).
[21] Randolph, A. and Clifford, M., *Int. J. Adhes. Adhes.* **24**, 389–405 (2004).
[22] Kumar, S. B., Sridhar, I., Sivashanker, S., Osiyemi, S. O., and Bag, A., *Mater. Sci. Eng.* **132**, 113–120 (2006).
[23] Zhang, Z. and Shang, J. K., *J. Adhesion* **49**, 23–36 (1995).
[24] Crobombe, A. D., Ong, C. Y., and Abdel-Wahab, M. M., *J. Adhesion* **78**, 745–776 (2002).
[25] Curley, A. J., Hadavinia, H., Kinloch, A. J., and Taylor, A. C., *Int. J. of Fracture* **103**, 41–69 (2000).
[26] Destrebecq, J. F., Grediac, M., and Sierra-Ruiz, V., *Compo. Sci. Technol.* **67**, 707–719 (2007).

[27] Hadavinia, H., Kinloch, A. J., Little, M. S. G., and Taylor, A. C., *Int. J. Adhes. Adhes.* **23**, 449–461 (2003).
[28] Saanouni, K. and Chaboche, J. L., *Numerical and Computational Methods* (De Borst and Mang, 2003), Vol. 3, Ch. 7.
[29] Lestriez, P., Saanouni, K., Mariage, J. F., and Cherouat, A., *Int. J. Damage Mech.* **13**, 59–80 (2004).
[30] Lestriez, P., Mariage, J. F., Saanouni, K., and Cherouat, A., *8th Int. Conf. Num. Meth. Indust. Forming Proc.* (Columbus, Ohio, 2004).
[31] Mendels, D.-A., Page, S. A., Leterrier, Y., Manson, J.-A. E., and Nairn, J. A., *ECCM'9*, Brighton, United Kingdom, (2000).
[32] Galerkin, B. G., *Vestn. Inghenerov.* **19**, 897–908 (1915).
[33] Jaumann, G., *Akad. Wiss. Wien Sitzber.* **120**, 385–530 (1911).
[34] Adkins, D. W. and Pipes, R. B., *Comp. Sci. Technol.* **22**, 209–221 (1985).
[35] Qian, Z. Q., Akisanya, A. R., and Imbabi, M. S., *Int. J. Solids Struct.* **37**, 5973–5994 (2000).